A&A 641, A179 (2020)
https://doi.org/10.1051/0004-6361/202038199

Astronomy & Astrophysics

Sensitivity of LEKID for space applications between 80 GHz and 600 GHz

A. Catalano[1], A. Bideaud[2], O. Bourrion[1], M. Calvo[2], A. Fasano[2], J. Goupy[2], F. Levy-Bertrand[2], J. F. Macías-Pérez[1], N. Ponthieu[3], Q. Y. Tang[2,4], and A. Monfardini[2]

[1] Univ. Grenoble Alpes, CNRS, LPSC/IN2P3, 38000 Grenoble, France
e-mail: catalano@lpsc.in2p3.fr
[2] Univ. Grenoble Alpes, CNRS, Grenoble INP, Institut Néel, 38000 Grenoble, France
[3] Univ. Grenoble Alpes, CNRS, IPAG, 38000 Grenoble, France
[4] Kavli Institute for Cosmological Physics, University of Chicago, 60637 Chicago, IL, USA

Received 17 April 2020 / Accepted 29 June 2020

ABSTRACT

We report the design, fabrication, and testing of lumped element kinetic inductance detectors (LEKID) showing performance in line with the requirements of the next generation space telescopes operating in the spectral range from 80 GHz to 600 GHz. This range is of particular interest for cosmic microwave background studies. For this purpose we designed and fabricated 100 pixel arrays covering five distinct bands. These wafers were measured via multiplexing, in which a full array is read out using a single pair of lines. We adopted a custom cold black body installed in front of the detectors and regulated at temperatures between 1 K and 20 K. In this paper, we describe in the main design considerations, fabrication processes, testing and data analysis.

Key words. instrumentation: detectors – cosmic background radiation – space vehicles: instruments – early Universe

1. Introduction

Instruments using kinetic inductance detectors (KIDs) have been demonstrated to reach the latest performance in the case of ground-based observations. The kilo-pixel, dual-band New IRAM Kids Arrays (NIKA2) camera was the first KID-based instrument operating at millimetre wavelengths. This camera showed that lumped element kinetic inductance detectors (LEKID) are limited by photon noise when they operate under an optical load typical of ground-based observations (Adam et al. 2018; Perotto et al. 2020). The last space-borne instrument devoted to cosmic microwave background (CMB) observations, *Planck*, has used 52 high-impedance spider-web bolometers in the high-frequency instrument (HFI) and has already shown their sensitivities were limited by CMB photon noise (Planck Collaboration I 2011; Planck Collaboration XVI 2014; Planck Collaboration I 2016; Planck Collaboration XIII 2016; Planck Collaboration X 2020). Even though HFI bolometers had the best sensitivity possible per pixel, after five full sky surveys, the CMB B-mode (Hu & White 1997) has been only marginal detected by *Planck*. For this reason, new proposed space missions (Lee 2016) and the upcoming CMB Stage IV ground experiments (Tsan & Simons Observatory Collaboration 2020; Carlstrom et al. 2019) aim to improve the overall noise equivalent power (NEP) of new instruments by increasing the focal plane coverage, using thousands of photon noise-limited contiguous pixels.

In this paper, we present our recent developments concerning the design, fabrication, and testing of complete arrays of LEKID operating between 80 GHz and 600 GHz under an optical loading typical of the space environment. This particular range of frequencies has been chosen because it includes the peak of the CMB emission (around 150 GHz), and it extends sufficiently to ensure an efficient measurement and subtraction of the foregrounds. In order to focus our efforts, the arrays were optimised for five different bands: 80–120 GHz (centred on 100 GHz), 120–180 GHz (centred on 150 GHz), 180–270 GHz (centred on 240 GHz), 320–400 GHz (centred on 360 GHz), and 450–650 GHz (centred on 550 GHz). Each array consists of around a hundred pixels and is multiplexed so that a single readout line can read out all the pixels on an array. In Sect. 2 we present the requirements and the experimental set-up. In Sect. 3 we illustrate the main design guidelines and the fabrication processes. In Sect. 4 we describe the laboratory tests, which permitted extensive device characterisation, in particular, in terms of the sensitivity, spectral, and dynamical performance.

2. Requirements and experimental set-up

When operated above the atmosphere, an instrument covering the band 80–600 GHz is loaded mostly by the 2.72 K CMB and the thermal radiation of the interstellar dust. In addition, above roughly 300 GHz, the instrument itself becomes an important source of optical background because of the thermal emission of the telescope (Planck Collaboration & Lawrence 2011). For typical configurations (e.g. *Planck*, LiteBIRD Lee et al. 2019, or in other works Baselmans et al. 2017, de Bernardis et al. 2018), the optical loading on a pixel is in the range 0.1–1 pW, depending on the observed bandwidth and other factors such as the instrumental throughput. The needed NEP is at least one order of magnitude lower compared to the ground-based case. For this work, we define our goal NEP per pixel as

$$\mathrm{NEP}_{\mathrm{goal}} \leq \sqrt{2} \cdot \mathrm{NEP}_{\mathrm{Phot}}, \quad (1)$$

where $\mathrm{NEP}_{\mathrm{Phot}}$ represents the source of noise related to the photon noise[1]. The quantity $\sqrt{2}$ means that we require that all the

[1] The photon noise comes from the intrinsic fluctuations of the incident radiation that are due to the Bose-Einstein distribution of the photon emission. In the best-case scenario, the contribution of photon noise is the limit of sensitivity of the instrument

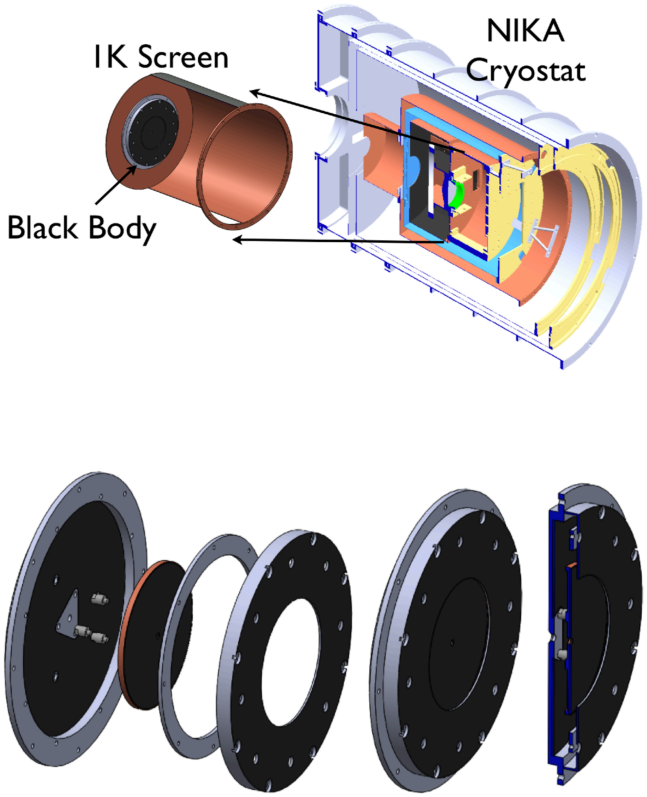

Fig. 1. *Top*: three-dimensional drawing of the dilution cryostat used for the tests. The black body is mounted at the end of the still screen, at a base temperature of around 1 K. *Bottom*: close-up view of the cryogenic back-body.

other sources of instrumental noise as random quasi-particle recombination, TLS noise (Flanigan et al. 2016), and pre-ampli noise to not exceed the photon noise level. When this condition is satisfied, we refer to the devices as photon-noise-dominated detectors.

In order to reproduce the particular conditions of optical power for each band, we used a dilution cryostat operating at 100 mK and equipped with a cryogenic black body installed on the 1 K (still) stage. The black body can be regulated, via a standard PID procedure, between 1 K and 20 K. This has no impact on the thermal stability of the coldest stage and the detectors. The black body (see Fig. 1) is composed of: (a) an aluminium support covered by black stycast glue, (b) three Vespel legs, (c) a copper disc covered by carbon-doped black stycast mixed with SiC grains, and (d) a metallic support to hold the band-defining filters. The copper disc, with its highly emissive coating, represents the actual black body. The performance of the coating has been compared with the commercial foam *Eccosorb AN-72*, rated for better than −17 dB reflectivity at ≥20 GHz. The measurement, performed at 150 GHz, shows comparable emissivity for both cases. The black-body geometry has been studied in order to minimise the thermal capacitance and ensure good isotherm behaviour of the emissive part. The Vespel legs have a purely mechanical role and present a negligible thermal conductance. A calibrated and easily replaceable thermal link is thus added to adjust the time constant. To avoid multiple reflections, which could lead to increase the final throughput, we fully coated the cryogenic screens between the black body and detectors. In addition, the 1-Kelvin (still) screen is optically closed with respect to the warmer screen to avoid stray lights.

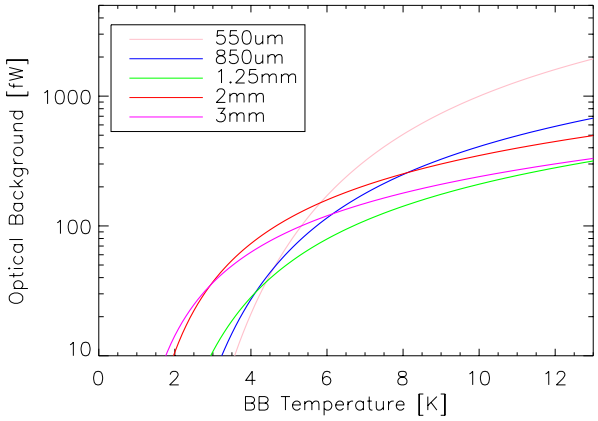

Fig. 2. Estimation of the optical power per pixel as a function of the temperature of the cold black body.

The five spectral bands are defined by low-pass, high-pass, or band-pass metal mesh filters. For the detectors covering the 3 mm and 2 mm bands the low-frequency cut-off is provided by the superconductor film itself (see Sect. 4.1).

The optical loading per pixel is equal to

$$W_{\rm pixel} = \tau \int_0^\infty {\rm A}\Omega\chi(\nu){\rm BB}(T,\nu)d\nu, \quad (2)$$

where the expression A · Ω is the throughput of the system. The quantity A is the area of the 100 mK cold stop, through which the black body is observed. The quantity Ω is the solid angle between the cold stop and the pixel.

τ is the overall transmission, mostly the transmission of the optical filters used to select the spectral bands. This parameter has been characterised by the Cardiff team who provided the filters and its value is between 90% and 95%. The typical out-of-band rejection, also confirmed by in-house measurements, is better than 1% per filter. The effective high-frequency rejection is further enhanced by the fact that these pixels, mostly optimised for millimetre waves, are by construction very poor terahertz absorbers.

$\chi(\nu)$ is the measured spectral band, normalised to 1 at the peak. By this normalisation we assume that the absorption is 100% at the peak. This assumptionwas demonstrated by reflection measurements using a network analyser, an rf set-up to provide the frequency band, a feed horn, a corrugated lens, and the array (with its back-short; Roesch et al. 2012).

BB(T,ν) is the brightness of the black body at the working temperature. We assume an ideal emissivity across the whole band.

In Fig. 2, we present the results of an optical simulation performed for this set-up. In particular, we show the optical power per pixel integrated in the specific spectral band.

3. Design and fabrication of the LEKID arrays

For this study, we specifically designed and fabricated arrays optimised for low background, i.e. 0.1–1 pW per pixel, and for five distinct spectral bands centred on wavelengths of 3, 2, 1.25, 0.85, and 0.55 mm. The final designs are the result of extensive electro-magnetic (transmission-line model, planar, and full 3-D) calculations and simulations. The detectors that we used are back-illuminated LEKID, i.e. LC resonators made by a long, meander inductor terminated at both ends by an inter-digitated capacitor. Most of the arrays are based on thin aluminium

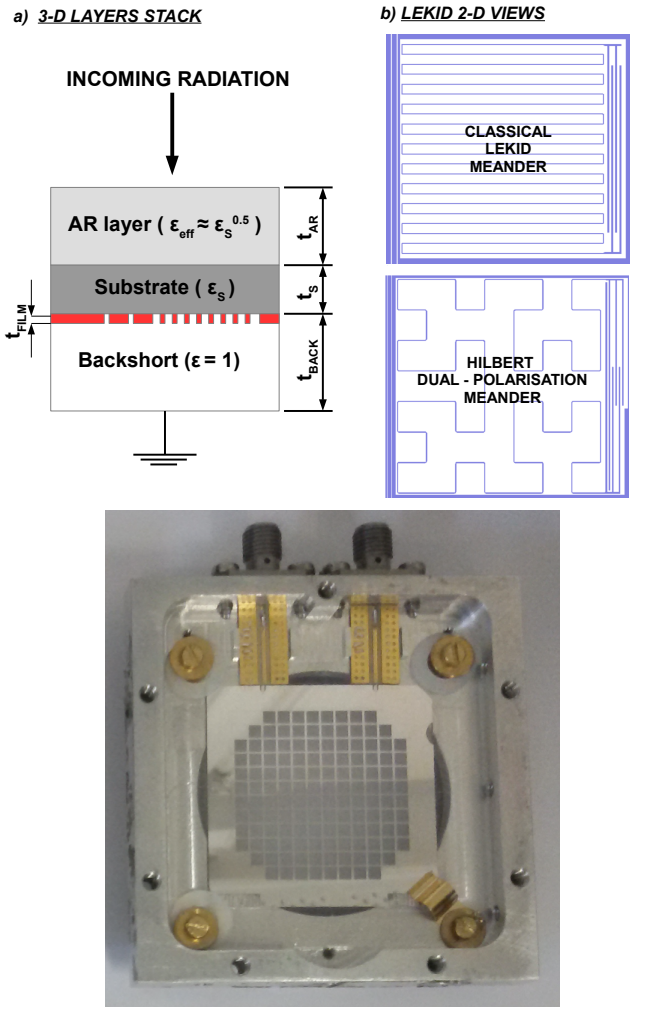

Fig. 3. (*a*) LEKID 3-D stack. In red, the superconducting film (thickness not to scale). The micromachined AR was made using only silicon substrates. The backshort lid is superconducting to avoid affecting the quality factor of the resonators. (*b*) The two kinds of planar LEKID designs adopted: the classical (CL) meander or the Hilbert (H) dual-polarisation structure. *Bottom panel*: picture of the final prototypes at 3 mm.

films ($t_{\rm FILM} = 15$–18 nm), with a critical temperature $T_c \approx 1400$ mK, corresponding to a lower frequency cut-off of about 110 GHz. On the other hand, the array operating at 3 mm employs a titanium-aluminium bi-layer film ($t_{\rm FILM} = 35$ nm, with $t_{\rm Ti} = 10$ nm and $t_{\rm Al} = 25$ nm) with $T_c = 900 \pm 25$ mK. For a standard Mattis-Bardeen superconductor, this results in a theoretical cut-off around 70 GHz (Catalano et al. 2015). The LEKID planar design is mostly based on results from adaptations and optimisations starting from the pixels elaborated for the NIKA instrument (Monfardini et al. 2011). Among the most important resonators parameters to be optimised out of planar simulations is the coupling quality factor of the resonators that has been adjusted, for the present study, to be in the range $Q_c \approx 5 \cdot 10^4$–10^5.

In the Fig. 3, we present the 3-D layout and examples of the LEKID planar views. As far as the optical coupling efficiency is concerned (left part of Fig. 3), the key variables to be calculated include the substrate (high-resistivity HR silicon or sapphire) thickness t_S, the thickness and effective dielectric constant of the anti-reflecting (AR) layer $t_{\rm AR}$, $\epsilon_{\rm AR}$ (only for silicon substrates), the thickness of the vacuum backshort $t_{\rm BACK}$, and the effective

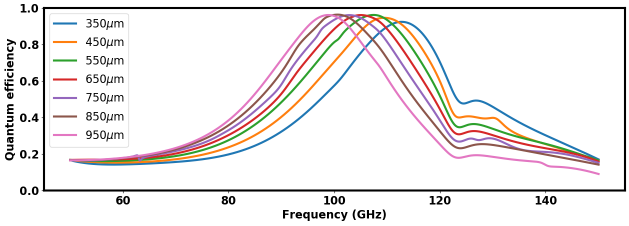

Fig. 4. Transmission-line model calculation to optimise, in terms of the pixel quantum efficiency, the backshort distance $t_{\rm BACK}$ for the 3 mm array. The optimum value is established at $t_{\rm BACK} \approx 750\,\mu$m.

Table 1. Main characteristics of the arrays.

Wavelength frequency	3 mm 100 GHz	2 mm 150 GHz	1.25 mm 240 GHz	850 μm 360 GHz	550 μm 550 GHz
Film material	Ti-Al	Al	Al	Al	Al
Film thickness [nm]	10–25	18	15	15	15
Critical temperature [K]	900	≈1.3	1.45	1.45	1.45
Substrate material	Al_2O_3	Al_2O_3	Si	Si	Si
Substrate thickness [μm]	430	330	280	265	170
AR layer thickness [μm]	0	0	110	110	80
Backshort thickness [μm]	750	670	530	350	400
LEKID meander type	CL	H	H	CL	CL
Pixel size [mm]	2.3	2.3	1	1	1
Design pixels/array [#]	132	132	132	128	128

impedance of the superconducting (Al or Ti-Al) film as seen by the incoming wave. This last parameter is strongly related to the superconducting material(s) properties and the thickness of the film $t_{\rm FILM}$. Figure 4 shows an example of a transmission-model estimation of the optical efficiency of the 3 mm array when varying $t_{\rm BACK}$.

The 2-D planar structures printed in the superconducting film (right part of Fig. 3) are designed to ensure a good optical coupling and satisfy the circuit requirements in terms, for example, of quality factor and resonance frequency f_0. For the present study, we adopted the resonance frequency range of $f_0 = 1$–3 GHz. The main geometrical characteristics of the arrays are presented in Table 1.

The fabrication process is similar for all arrays. The substrate (either HR Si or C-cut Al_2O_3) is prepared by applying an HF vapour cleaning. The superconducting film is deposited by e-beam evaporation and under a residual chamber pressure of $5{\cdot}10^{-8}$ mbars. In the case of the 3 mm array, the titanium (first) and aluminium (second) layers are deposited in sequence without breaking the vacuum. The deposition rates are within the range 0.1–0.5 nm s^{-1}. This procedure guarantees a clean interface, and the protection of the (underlying) titanium layer when the chip is exposed to the atmosphere.

The UV photo-lithography step is achieved using a positive resist, and is followed by wet etching using a standard aluminium etching solution based on a diluted H_3PO_4/HNO_3 mixture. A dip in 0.1% HF, to etch the underlying titanium film, is added for the 3 mm array case. The arrays made on silicon substrates undergo the AR-layer step by dicing, on the back of the Si wafer, a regular cross-pattern of grooves (Goupy et al. 2016).

The diced and eventually AR-coated detectors are packaged in custom holders and bonded using superconducting aluminium wires (dia. 17 μm). The detector is connected via SMA connectors to high-quality coaxial cables and a cold low-noise amplifier to be read out with the external multiplexing circuit (Bourrion et al. 2012).

Table 2. Main results of the paper: optical power, noise, and derived NEP for a given optical load corresponding to the typical space environment.

Wavelength frequency	3 mm 100 GHz	2 mm 150 GHz	1.25 mm 240 GHz	850 μm 360 GHz	550 μm 550 GHz
Optical load [pW/pixel]	0.09	0.11	0.14	0.18	1.2
T_{BB} [K]	5	5	8	7	11
Averaged optical resp [kHz/fW]	2.3	0.78	1.1	0.84	0.19
Averaged noise (1–10 Hz) [Hz/ $\sqrt{\text{Hz}}$]	6	3	6.5	5.5	4
NEP [aW/ $\sqrt{\text{Hz}}$]	2.6 ± 0.4	4.0 ± 0.4	5.5 ± 0.5	5.2 ± 1.1	23 ± 3.5
NEP_{Phot} [aW/ $\sqrt{\text{Hz}}$]	2.45	3.4	4.8	5.0	21

Notes. The averaged optical response and noise is derived over the best 30% of the pixels for the arrays at 3 mm, 2 mm, and 1.25 mm. In the case of 850 μm and 550 μm arrays, the best 10% of the pixels are considered. The NEP_{Phot} is calculated from the photon noise at the given optical load.

4. Detectors characterisation

The arrays described in Sect. 3 were first tested with the cryostat closed and the detectors illuminated by the cold black body (see Sect. 2). The results of these measurements are shown in Sects. 4.1 and 4.4. We spectrally characterised the very same arrays to correctly establish a NEP calculation. For this measurement, the full cryostat optics is installed and the camera is interfaced with the Fourier transform interferometer. These experiments are described in more detail in Sect. 4.2. In addition, the 3 mm array was tested with our fast, i.e. 1 MHz sampling, homodyne electronics to determine the LEKID response time constant (see Sect. 4.3). For space instruments that are exposed to a considerable flux of primary cosmic rays, the response time is a crucial parameter (Masi et al. 2019; Catalano et al. 2016).

4.1. Resonators electrical properties characterisation

The 132 LEKID of the 3 mm (Ti-Al, $t_{\text{FILM}} = 10$–25 nm) and 2 mm (Al, $t_{\text{FILM}} = 18$ nm) arrays (pixels size 2.3 mm) resonate between 1.4 GHz and 1.9 GHz. The arrays have average internal quality factors of 4.8×10^4 and 6.2×10^4, respectively, under typical CMB loading (see first raw in Table 2). The critical temperature of the Ti-Al film has been roughly estimated, in this case, by monitoring the readout line transmission, at around 900 mK. The transition is crossed multiple times in both ways (warming-up and cooling-down) to exclude potential thermal drifts. This value is in agreement with previous measurements on similar films (Catalano et al. 2015).

The normal-state sheet resistance of the Ti-Al bi-layer was independently measured at $T = 1$ K to be $R_N^{\text{Ti-Al}} = 0.5\,\Omega\,\text{square}^{-1}$. The 132 LEKID of the 1 mm (Al, $t_{\text{FILM}} = 15$ nm) array (pixels size 1 mm) resonates between 1.7 GHz and 2.1 GHz. These detectors were measured to have an average internal quality factor of 5.0×10^4. The superconducting transition temperature of the 15 nm film is 1450 ± 50 mK, while the normal-state sheet resistance is $R_N^{\text{Al}} = 2\,\Omega\,\text{square}^{-1}$.

The normal-state sheet resistance (measured) is related to the critical temperature (measured) and the surface inductance through the relation Leduc et al. (2010), $L_s = \frac{\hbar R_s}{\pi \Delta}$, where Δ is the superconducting gap equal to $\Delta = 1.764 \cdot k_B \cdot T_c$ for BCS ideal superconductors. The surface inductance was estimated from electro-magnetic simulation to explain the observed position of the fundamental resonance frequency. In the case of the Ti-Al film, we found $L_s \approx 1\,\text{pH square}^{-1}$. The three electrical values (Δ, L_s and R_s), measured or estimated with independent methods, satisfy the cited relation within 10%.

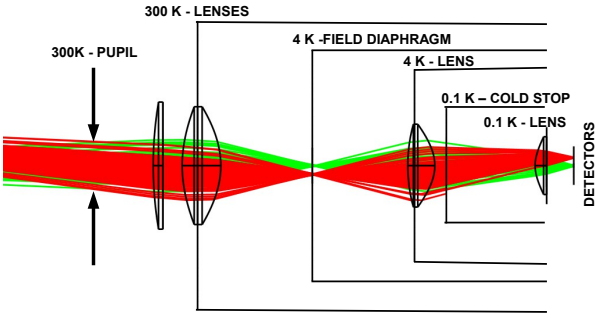

Fig. 5. Scheme of the optics adopted for the spectral characterisation. The lenses are made out of HDPE (high density polyethylene). The low-pass and thermal filters positions are not shown. The interferometer input window is located at the 300 K pupil position.

4.2. Spectral characterisation

The spectral response was measured using a custom built Martin-Puplett interferometer (MpI) interfaced to the camera (cryostat) containing the detectors. The optics configuration for this measurement is shown in Fig. 5. Infrared-blocking filters are installed on the 300 K, 150 K, and 50 K cryogenics stages. Metallic multi-mesh, low-pass filters are placed at 50 K, 4 K, and 1 K. The band-defining filters, again metallic multi-meshes, are installed at base temperature, i.e. around 100 mK, in front of the array.

We modulated the input signal between two distinct Rayleigh-Jeans spectrum sources held at different temperatures to maximise the signal-to-noise ratio of the interferogram. The modulation is achieved by a rotating wire-grid polariser, which also produces the fully polarised input signal. The signal is then extracted with a standard lock-in detection.

The measured band transmissions are presented in Fig. 6. The five spectral bands span the whole range of frequencies from 70 GHz up to 630 GHz, via adjacent bands with a relative full width at half maximum (FWHM) between 15% and 30%. The relative bandwidths are mostly limited by the optical filters that were available. The spectral features are well understood and in agreement with 3-D electro-magnetic simulations, when taking into account the full detectors structure. If required by the end application, the spectral curves might be designed to be smoother. For the present study, we instead optimised the amplitude of the absorption peak.

4.3. Dynamical response characterisation

In order to measure the characteristic response time of LEKID under typical CMB radiation loading, we recorded some fast

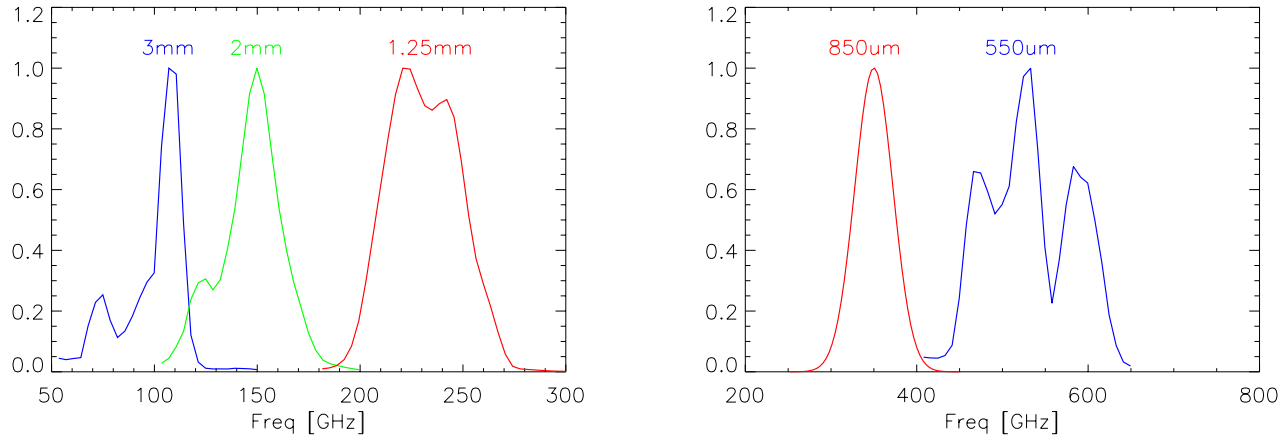

Fig. 6. Normalised spectral response for the 5 arrays (Si/max(Si), where Si is the averaged response of the pixels). The dispersion level between pixels is of the order of a few percent. The dip at 556 GHz is an artefact related to a strong and well-known water vapour absorption line.

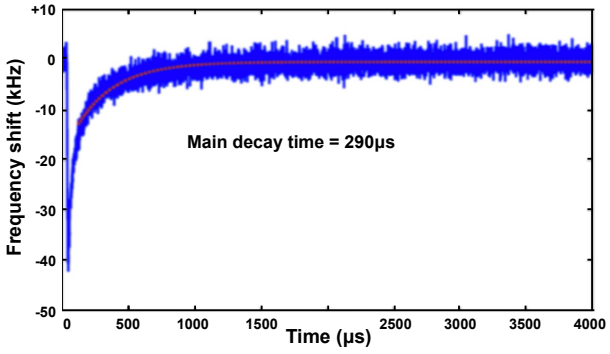

Fig. 7. One representative cosmic-ray (muon) pulse showing a main decay time of around 0.3 ms. Trace recorded by fast (1 MHZ sampling) homodyne electronics on a typical LEKID of the 3 mm array (Ti-Al film). The array was operated under typical CMB optical background.

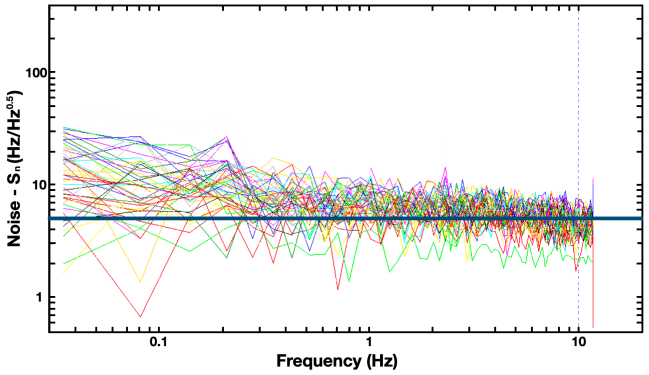

Fig. 8. Noise density for all the pixels of the 2 mm array. Measured with a cold black-body temperature of 6 K. The blue line represents the average noise level after common mode decorrelation.

high-energy events on the 3 mm array. These events are generated by secondary cosmic rays (muons) reaching the ground and crossing the monocrystalline substrate. As a result of this ionising track, a-thermal ballistic phonons are generated in the crystal. A fraction of these phonons are energetic enough to break Cooper pairs in the superconductor film, generating lossy quasi-particles and changing the kinetic inductance of the resonator (Swenson et al. 2010). By fitting the decay time of the spikes, we derived the quasi-particles recombination time constant in the Ti-Al film that coincides, for these pair-breaking detectors, with the response time. We present a typical cosmic-ray event in Fig. 7. The energy deposited by the muon in the substrate is of the order of hundreds of keV. As already shown for example in Karatsu et al. (2019) and Catalano et al. (2016), we know that the impact of cosmic rays in KID detectors is mitigated with respect to thermal detectors by the fact that when a particle hit occurs only about 1% of the absorbed energy is used to break Cooper pairs and therefore to generate a measurable signal. Considering the full sample of recorded pulses, and fitting for each decay constant, we measure $\tau_{\rm response} = 290 \pm 35\,\mu$s. As expected, this time constant is higher than that seen on the same kind of pixels operating under higher loading, i.e. higher density of quasi-particles. For example, in the past observed shorter time constants of the order of tens of microseconds under typical ground-based backgrounds. However, a time constant of around 0.3 ms is still fast enough for a CMB space-borne mission without introducing significant systematic errors (Catalano et al. 2016; Monfardini et al. 2016).

4.4. Sensitivity characterisation

The response of each detector (pixel) was measured by performing, under stable conditions and for several black-body temperatures ($T_{\rm BB}$), frequency sweeps to measure the LEKID transfer function ($\frac{\Delta f}{\Delta T_{\rm BB}}$). The pixel responsivity is then obtained as the ratio of the frequency shift to the corresponding change of the optical background as follows:

$$\Re{\rm esp}(T_{\rm BB}) = \frac{\Delta f}{\Delta W_{\rm opt}},$$

where $W_{\rm opt}$ is derived from the model presented in Sect. 2. In parallel, we measured the spectral frequency noise density $S_n(f)$, expressed in Hz/$\sqrt{\rm Hz}$, for each $T_{\rm BB}$. In Fig. 8 we show a typical noise (raw) measured for the 2 mm array and with $T_{\rm BB} = 6$ K. The correlated electronic noise is removed by subtracting a common mode obtained by averaging the time-ordered data (TOD) of all detectors. The resulting template is fitted linearly to each TOD. The best fit is then subtracted from the detector TOD. After decorrelation, the spectral noise density is nicely flat in the band 1–10 Hz. Depending on the array and $T_{\rm BB}$, the frequency noise level sits between 2 and 10 Hz/$\sqrt{\rm Hz}$. The NEP is then

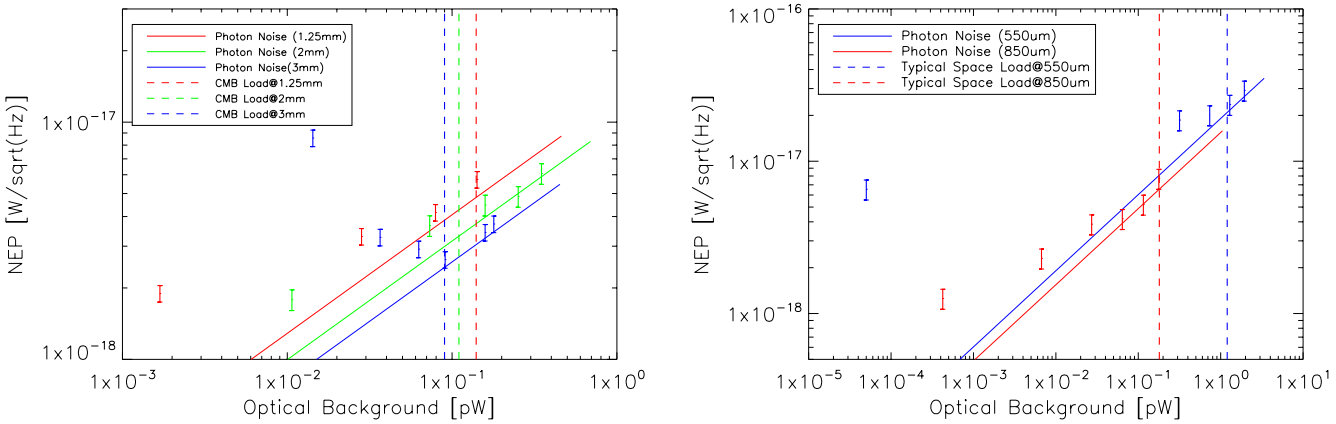

Fig. 9. Noise equivalent power (NEP) measured for the 1 mm, 2 mm, and 3 mm arrays. Each point is derived from responsivity and noise measurements for different temperatures of the cold black body. The corresponding optical load per pixel for each temperature is derived using the optical simulation presented in Fig. 2. The vertical dashed lines represent the typical optical background expected from a real instrument operating at second Lagrangian point.

derived as

$$\mathrm{NEP} = \frac{S_n(f)}{\mathfrak{R}\mathrm{esp}}.$$

Figure 9 shows the NEP for all the arrays and as a function of the optical background. We compare these results to the corresponding expected $\mathrm{NEP}_{\mathrm{Phot}}$ derived for CMB in a space environment (see also Table 2). The results indicate that the NEPs approach the goal (defined in Eq. (1)), in the range of CMB loading, for all the arrays (bands) presented in this paper. For higher optical loads the measured NEP scale correctly. For lower optical loads, on the other hand, the expected NEP scaling with the theoretical photon noise is not respected. This is likelybecause our optical set-up might introduce an additional background when running at femto-Watts per-pixel levels. A deeper investigation of this regime of backgrounds is beyond the scope of the present study.

5. Conclusions

We have extensively characterised LEKID arrays optimised to work within five bands suitable for CMB space observations. We elaborated on standard measurement protocols allowing us to potentially test a large number of arrays in a reproducible and documented way. This is extremely important in the research and development phase in which new materials and designs have to be compared to identify promising recipes. Adopting this same protocol, we tested the arrays covering the band 70–630 GHz. All the LEKID arrays seem to satisfy the stringent requirements, in terms of sensitivity, of post-*Planck* satellites dedicated to CMB polarisation studies.

The future generation space instruments devoted to CMB studies will employ thousands of pixels. Based on this study, that is fully multiplexed 100-pixel-like arrays similar run under realistic conditions, the scaling to the final number of pixels seems straightforward. The next step of the research and development phase will be therefore to improve the homogeneity within the arrays.

Acknowledgements. The engineers more involved in the experimental setup development are G. Garde, H. Rodenas, J.-P. Leggeri, M. Grollier, G. Bres, C. Vescovi, J.-P. Scordilis, E. Perbet. We acknowledge the crucial contributions of the whole Cryogenics and Electronics groups at Institut Néel and LPSC. The arrays described in this paper have been produced at the PTA Grenoble microfabrication facility. This work has been funded by CNES under an R&T contract; we thank H. Geoffray and P.-G. Tizien. QYT was partially supported by the UChicago-CNRS fund.

References

Adam, R., Adane, A., Ade, P. A. R., et al. 2018, A&A, 609, A115
Baselmans, J. J. A., Bueno, J., Yates, S. J. C., et al. 2017, A&A, 601, A89
Bourrion, O., Vescovi, C., Bouly, J. L., et al. 2012, J. Instrum., 7, 7014
Carlstrom, J., Abazajian, K., Addison, G., et al. 2019, BAAS, 51, 209
Catalano, A., Goupy, J., le Sueur, H., et al. 2015, A&A, 580, A15
Catalano, A., Benoit, A., Bourrion, O., et al. 2016, A&A, 592, A26
de Bernardis, P., Ade, P. A. R., Baselmans, J. J. A., et al. 2018, JCAP, 2018, 015
Flanigan, D., McCarrick, H., Jones, G., et al. 2016, Appl. Phys. Lett., 108, 083504
Goupy, J., Adane, A., Benoit, A., et al. 2016, J. Low Temp. Phys., 184, 661
Hu, W., & White, M. 1997, Phys. Rev. D, 56, 596
Karatsu, K., Endo, A., Bueno, J., et al. 2019, Appl. Phys. Lett., 114, 032601
Leduc, H. G., Bumble, B., Day, P. K., et al. 2010, Appl. Phys. Lett., 97, 102509
Lee, A. T. 2016, in American Astronomical Society Meeting Abstracts #228, Am. Astron. Soc. Meeting Abstr., 228, 301.08
Lee, A., Ade, P. A. R., Akiba, Y., et al. 2019, BAAS, 51, 286
Masi, S., de Bernardis, P., Paiella, A., et al. 2019, JCAP, 2019, 003
Monfardini, A., Benoit, A., Bideaud, A., et al. 2011, ApJS, 194, 24
Monfardini, A., Baselmans, J., Benoit, A., et al. 2016, in Lumped Element Kinetic Inductance Detectors for Space Applications, SPIE Conf. Ser., 9914, 99140N
Perotto, L., Ponthieu, N., Macías-Pérez, J. F., et al. 2020, A&A, 637, A71
Planck Collaboration & Lawrence, C. R. 2011, in American Astronomical Society Meeting Abstracts #217, Am. Astron. Soc. Meeting Abstr., 217, 243.04
Planck Collaboration I. 2011, A&A, 536, A1
Planck Collaboration XVI. 2014, A&A, 571, A16
Planck Collaboration I. 2016, A&A, 594, A1
Planck Collaboration XIII. 2016, A&A, 594, A13
Planck Collaboration X. 2020, A&A, 641, A10
Roesch, M., Benoit, A., Bideaud, A., et al. 2012, ArXiv e-prints [arXiv:1212.4585]
Swenson, L. J., Cruciani, A., Benoit, A., et al. 2010, Appl. Phys. Lett., 96, 263511
Tsan, T., & Simons Observatory Collaboration 2020, in American Astronomical Society Meeting Abstracts, Am. Astron. Soc. Meeting Abstr., 235.04